International Journal of Nanomedicine

Dovepress
Taylor & Francis Group

Open Access Full Text Article

ORIGINAL RESEARCH

Enhanced NIR-II Nanoparticle Probe for PSMA-Targeted Molecular Imaging and Prostate Cancer Diagnosis

Zhongji Jiang[1,2], Jin Zhang[3], Jiali Jin[3], Xun Zhang[4], Gaohaer Kadeerhan[5], Hong Guo[3], Dongwen Wang[2,6]

[1]Department of Biology, School of Medicine, Southern University of Science and Technology, Shenzhen, Guangdong, 518055, People's Republic of China; [2]Department of Urology, National Cancer Center/National Clinical Research Center for Cancer/Cancer Hospital & Shenzhen Hospital, Chinese Academy of Medical Sciences and Peking Union Medical College, Shenzhen, Guangdong, 518116, People's Republic of China; [3]Department of Urology, First Hospital of Shanxi Medical University, Taiyuan, Shanxi, 030001, People's Republic of China; [4]Department of Materials Science and Engineering, Southern University of Science and Technology, Shenzhen, Guangdong, 518055, People's Republic of China; [5]Central Laboratory, National Cancer Center/National Clinical Research Center for Cancer/Cancer Hospital & Shenzhen Hospital, Chinese Academy of Medical Sciences and Peking Union Medical College, Shenzhen, Guangdong, 518116, People's Republic of China; [6]School of Medicine, Southern University of Science and Technology, Shenzhen, Guangdong, 518055, People's Republic of China

Correspondence: Dongwen Wang, Email urology2007@126.com

Introduction: Prostate-specific membrane antigen (PSMA) is a well-established biomarker overexpressed in prostate cancer (PCa). However, existing PSMA-targeted imaging probes suffer from radiation exposure, limited tissue penetration, and inadequate intraoperative performance. To overcome these challenges, we developed a novel near-infrared-II (NIR-II) fluorescent nanoprobe for both in vivo and ex vivo imaging of PCa.

Methods: An organic semiconducting polymer (OSP_{12}) with strong NIR-II fluorescence and excellent photostability was self-assembled into nanoparticles (NPs) using DSPE-PEG-Mal. These OSP_{12} NPs were then conjugated with ACUPA-SH, (S)-2-[3-((S)-5-amino-1-carboxypentyl)ureido]pentanedioic acid, a thiol-modified glutamate-urea-lysine derivative that specifically targets PSMA, via a maleimide-thiol click reaction to form PSMA-OSP_{12} NPs. The probe's targeting specificity was assessed using PSMA positive and negative cell lines under NIR-II imaging. For in vivo evaluation, subcutaneous xenograft tumors were established in BALB/c nude mice. Animals were randomly assigned to PSMA-OSP_{12} NP, blocking (ACUPA pre-injection), and control (OSP_{12} NPs) groups (n = 3 per group). Ex vivo tumor slice imaging was performed on fresh tissue sections. Biosafety was evaluated in healthy mice (n=5) through hematological, biochemical, and histopathological analyses.

Results: PSMA-OSP_{12} NPs exhibited excellent optical properties in the NIR-II window, including high photostability, negligible autofluorescence, and deep tissue penetration. In vitro assays confirmed selective binding to PSMA-positive cells, while in vivo imaging demonstrated sustained tumor accumulation with a peak TBR of 7.40 ± 1.28 at 48 h post-injection. This performance significantly surpassed OTL78 and Cy-KUE-OA, enabling flexible surgical planning and real-time intraoperative guidance. In ex vivo tissue imaging, PSMA-OSP_{12} NPs provided high-contrast tumor delineation without systemic administration. Biosafety evaluations revealed no significant systemic toxicity, and biodistribution analysis indicated hepatic metabolism and biliary clearance.

Conclusion: PSMA-OSP_{12} NPs are a promising NIR-II fluorescent probe with excellent tumor specificity, deep tissue imaging capability, and good biocompatibility, supporting their application in fluorescence-guided surgery and ex vivo tumor evaluation.

Keywords: prostate cancer, prostate-specific membrane antigen, NIR-II, fluorescence-guided surgery, tumor targeting, molecular imaging, organic semiconducting polymer, nanoparticles

Introduction

Prostate cancer (PCa) is one of the most common malignancies in men and a major cause of cancer-related deaths globally.[1] Its incidence is several-fold higher in developed countries than in low- and middle-income countries (LMICs), primarily due to differences in access to prostate-specific antigen (PSA) screening and advanced imaging technologies.[2–4]

Received: 2 April 2025
Accepted: 28 July 2025
Published: 9 August 2025

While modalities such as Magnetic Resonance Imaging (MRI) and Positron Emission Tomography (PET) facilitate early diagnosis and intervention in high-resource settings, delayed diagnosis remains common in LMICs owing to limited healthcare infrastructure.[5,6] These disparities highlight the need for innovative, affordable, and precise imaging tools to enhance early detection, surgical guidance, and treatment monitoring of PCa.

Prostate-specific membrane antigen (PSMA), a type II transmembrane glycoprotein, is significantly overexpressed in most PCa and has become a validated molecular target for both imaging and therapy.[7] In 2020, the FDA approved ^{68}Ga-PSMA-11 as the first PET imaging agent for PCa.[8] Subsequently, in 2022, ^{177}Lu-PSMA-617 (Pluvicto) was approved for the treatment of metastatic castration-resistant PCa (mCRPC).[9] However, these agents rely on ionizing radiation, which poses safety concerns and provides limited spatial resolution, thereby restricting their applicability for real-time surgical navigation or optical pathological assessment.

Although PSMA-617 and PSMA-11 both share the glutamate-urea-lysine pharmacophore, their physicochemical characteristics limit further adaptation into nanoprobe platforms. PSMA-617 is highly hydrophobic and lacks suitable functional groups for conjugation, while PSMA-11 incorporates large chelating moieties that can hinder surface modification and compromise probe assembly.[10] In contrast, ACUPA (2-(3-((S)-5-amino-1-carboxypentyl) ureido) pentanedioic acid)—a glutamate-urea-based ligand engineered with a reactive thiol group—retains high affinity for PSMA and allows site-specific conjugation to nanoparticles via thiol–maleimide chemistry.[11,12] This structural simplicity and functional accessibility make ACUPA particularly suitable for the construction of targeted nanoprobes with enhanced stability and biocompatibility.

Molecular imaging enables non-invasive, dynamic visualization of physiological and pathological processes at the molecular level both in vivo and in freshly excised ex vivo specimens.[13,14] Fluorescence imaging, particularly in the near-infrared (NIR) spectrum, has emerged as a powerful complement to conventional modalities such as ultrasound, MRI, and PET.[15,16] Compared to visible light (400–700 nm) and NIR-I (700–900 nm), NIR-II fluorescence imaging (1000–1700 nm) offers markedly reduced tissue scattering, minimal autofluorescence, and superior penetration depth, achieving subcellular resolution at centimeter-scale tissue depths.[17–19]

Recent studies have demonstrated that conjugation of specific molecular targets with NIR fluorophores enables precise imaging of cancerous lesions, including PCa, in both live animal models and excised tissues.[17,19–26] Despite this promise, PSMA-targeted probes operating in the NIR-II window remain scarce. Most clinically explored agents, such as OTL-78 and Cy-KUE-OA, emit in the NIR-I range, limiting their efficacy in deep-tissue applications.[27,28] In contrast, organic semiconducting polymers (OSPs) like OSP_{12} exhibit high quantum yield, tunable emission properties, and photostability, making them ideal candidates for constructing next-generation NIR-II imaging probes.[29]

In this study, we developed a novel PSMA-targeted NIR-II fluorescent nanoprobe, PSMA-OSP_{12} nanoparticles (NPs), by covalently conjugating ACUPA to an OSP_{12}-based polymer micelle via thiol–maleimide click chemistry using DSPE-PEG-Mal. This design enables simultaneous integration of high tumor specificity, strong NIR-II emission, and excellent biocompatibility. We systematically characterized its physicochemical properties, in vitro and in vivo targeting capabilities, biodistribution, and biosafety. Furthermore, we demonstrated its applicability for intraoperative fluorescence navigation and ex vivo pathological visualization, addressing key limitations in current PCa imaging strategies.

Materials and Methods

Patient Samples

Three PCa patients, diagnosed postoperatively via pathological examination, provided paraffin-embedded tissue sections of tumor and adjacent normal tissue. Hematoxylin and eosin (HE) staining and PSMA immunohistochemical (IHC) staining (PSMA/GCPII antibody, 13163-1-AP, Proteintech, USA) were performed to assess PSMA protein expression levels. The study was conducted in accordance with the Declaration of Helsinki, and the protocol was approved by the Ethics Committee of the Ethics Committee of Shenzhen Hospital, Chinese Academy of Medical Sciences (JS2024-7-1).

Databases and Bioinformatics Analyses

TIMER 2.0 (http://timer.cistrome.org/): A comprehensive online database based on TCGA and other datasets, used to analyze the expression differences of PSMA (FOLH1) across 32 types of tumors, including prostate cancer.[30]

Prostate Cancer Atlas (https://prostatecanceratlas.org/): This database integrates RNA sequencing data from PCa samples, enabling pseudotime trajectory analysis to investigate disease progression from normal tissue to localized and metastatic tumors.[31] In this study, we used it for pseudotime trajectory analysis and to examine the expression differences of PSMA across different molecular types of PCa.

GEPIA2 (http://gepia.cancer-pku.cn/index.html): GEPIA2 is an interactive database combining TCGA and GTEx datasets, comprising 9736 tumor and 8587 normal samples. In this study, it was used to analyze the prognostic impact of PSMA expression on PCa overall survival (OS) and disease-free survival (DFS).[32]

Synthesis of PSMA-OSP_{12} NPs NIR-II Probe

The NIR-II fluorescent polymer OSP_{12} was synthesized as previously described.[29] For nanoprobe preparation, 10 mg of DSPE-PEG(2000)-Maleimide (1,2-distearoyl-sn-glycero-3-phosphoethanolamine-N-[maleimide(polyethylene glycol)-2000], DSPE-PEG-Mal, C139H271N4O57P, Avanti Polar Lipids, USA) and 1 mg of OSP12 were co-dissolved in tetrahydrofuran (THF, analytical grade, Sigma-Aldrich) and rapidly added into 10 mL of deionized water under continuous sonication (Branson 2510, USA) for 20 minutes. The resulting dispersion was dialyzed against deionized water (MWCO 8–14 kDa, Spectrum Labs, USA) for 24 h, filtered through a 0.22 μm PES membrane (Millipore, USA), and concentrated to 5 mL using centrifugal ultrafiltration (Corning® Spin-X, MWCO 3 kDa, 3000 rpm, 5 min). To introduce the targeting ligand, 1.5 mg of ACUPA-SH (S)-2-[3-((S)-5-amino-1-carboxypentyl)ureido]pentanedioic acid with a terminal thiol group, $C_{17}H_{29}N_3O_6S$, MW 407.44, New Research Biosciences, China) and 500 μL of 10× PBS (pH 7.4) were added to the dispersion and stirred overnight at 4 °C in the dark. The thiol–maleimide reaction enabled efficient coupling, and the final PSMA-OSP_{12} NPs were purified by centrifugation and resuspended in PBS.

The excitation and emission spectra of PSMA-OSP_{12} NPs were recorded using a fluorescence spectrometer (FLS1000, Edinburgh Instruments, UK). For in vitro NIR-II fluorescence imaging, three formulations—ACUPA-SH, OSP_{12} NPs, and PSMA-OSP_{12} NPs—were diluted to 100 μg/mL in deionized water and loaded into 1.5 mL Eppendorf tubes. To assess concentration-dependent fluorescence properties, PSMA-OSP_{12} NPs were further diluted to final concentrations of 10, 20, 40, 80, and 160 μg/mL and imaged under LP filters at 1000, 1100, 1200, and 1300 nm, respectively.

All fluorescence imaging, captured using an InGaAs camera (NIRvana 640, Princeton Instruments, USA), was performed under standardized conditions using an 808 nm continuous-wave diode laser with a power density of 60 mW/cm² and an exposure time of 100 ms. Long-pass (LP) filters at 1000–1300 nm were employed depending on experimental needs. All raw fluorescence images were acquired without post-acquisition enhancement, contrast adjustment, or pixel-wise background subtraction to ensure data authenticity and reproducibility. For quantitative analysis, regions of interest (ROIs) were manually delineated over tumors and representative background organs using Fiji-ImageJ (NIH, USA). The mean fluorescence intensity (MFI) within each ROI was measured and used to calculate imaging contrast metrics.

PSMA Binding Specificity Assay

To evaluate the binding specificity of PSMA-OSP_{12} NPs, a cell-based NIR-II fluorescence imaging assay was performed using PSMA-positive and PSMA-negative prostate cancer cell lines. PSMA-positive 22Rv1 cells and PSMA-negative PC-3 cells were seeded into black, clear-bottom 96-well plates (Corning®) at a density of 1×10^4 cells per well and cultured overnight at 37 °C in a humidified 5% CO_2 incubator.

Cells were divided into four treatment groups: Control 1: PC-3 cells incubated with PSMA-OSP_{12} NPs (10–160 μg/mL); Control 2: 22Rv1 cells incubated with non-targeted OSP_{12} NPs (10–160 μg/mL); Blocking group: 22Rv1 cells pretreated with ACUPA-SH (10 μM, 1 h),[28] followed by incubation with PSMA-OSP_{12} NPs (10–160 μg/mL); Experimental group: 22Rv1 cells directly incubated with PSMA-OSP_{12} NPs (10–160 μg/mL). All groups were incubated at 37 °C for 24 hours. After incubation, cells were washed three times with PBS to remove unbound materials. Each condition was performed in triplicate (n = 3), and statistical analysis was conducted using two-way ANOVA.

In vivo Fluorescence Imaging and Biodistribution in Xenograft Models

Male BALB/c nude mice (4–6 weeks old, purchased from Viton Lihua, Foshan, China) were used to establish subcutaneous prostate cancer xenografts. A total of 1×10^7 22Rv1 cells suspended in PBS containing 25% Matrigel

(Corning, Cat# 354237) were injected into the right flank of each mouse. Tumor volumes were calculated using the formula $V = ab^2 / 2$, where a and b denote the long and short diameters of the tumor. When tumors reached approximately 300 mm^3, mice were randomized into three groups (n = 3 per group): Control group: injected with non-targeted OSP_{12} NPs; Blocking group: pre-treated with ACUPA-SH (10 mM) 1 hour prior to PSMA-OSP_{12} NPs administration;[33,34] Experimental group: injected with PSMA-OSP_{12} NPs alone. Each mouse received 200 μL of 1 mg/mL nanoprobe solution via tail vein injection. In vivo NIR-II fluorescence imaging was performed using an InGaAs camera with 808 nm laser excitation, 1100 nm long-pass filter, and 100 ms exposure time at 10 min, 4 h, 12 h, 24 h, and 48 h post-injection. Additionally, at 30 h, animals were imaged under different spectral filters to assess tissue penetration and emission profiles. Tumor-to-Background Ratio (TBR) and Tumor-to-Liver Ratio (TLR) were calculated as: TBR = MFI_tumor / MFI_background; TLR = MFI_tumor / MFI_liver.

Ex vivo Tumor Imaging of PSMA-OSP_{12} NPs

To evaluate the tumor-targeting capability of PSMA-OSP_{12} NPs under controlled ex vivo conditions, an NIR-II fluorescence imaging assay was performed on tumor tissue slices. A total of six tumor-bearing mice were randomly divided into two groups (n = 3 per group). After excision, tumors were immediately sliced into approximately 2 mm thick sections using a sterile blade under cold PBS. Slices were transferred into plates and blocked with 5% fetal bovine serum (FBS) for 10 minutes at room temperature to reduce nonspecific binding. The samples were then incubated with either PSMA-OSP_{12} NPs or non-targeted OSP_{12} NPs at a final dye concentration of 200 μg/mL in PBS for 2 hours at room temperature in the dark. Following incubation, tumor slices were washed thoroughly three times with PBS to remove unbound nanoparticles. Quantitative fluorescence values were compared between groups using Student's *t*-test.

Biosafety Evaluation of PSMA-OSP_{12} NPs

To assess the biosafety of PSMA-OSP_{12} NPs, a series of in vivo experiments were conducted. Male BALB/c nude mice were randomly divided into two groups (n=5 per group): one receiving PSMA-OSP_{12} NPs (1 mg/mL, 200 μL) and the other receiving an equivalent volume of PBS as a control. The following parameters were evaluated:

Body Weight: Mice were monitored for changes in body weight from day 0 to day 14 post-injection, with measurements taken every two days to evaluate systemic toxicity; Hematological and Serum Biochemical Analysis: Blood samples were collected via the tail vein at days 0, 7, and 14 post-injection to measure red blood cell count (RBC), white blood cell count (WBC), platelet count (PLT), alanine aminotransferase (ALT), aspartate aminotransferase (AST), albumin (ALB), blood urea nitrogen (BUN), and creatinine (CREA). These parameters were used to assess potential effects on hematological, hepatic, and renal functions; Histopathological Analysis: At day 14, mice were euthanized, and major organs (heart, liver, spleen, lung, and kidney) were harvested for HE staining to evaluate pathological changes. All animal experiments were performed in accordance with the Guidelines for the Care and Use of Laboratory Animals and approved by the Animal Ethics Committee (TOPGM-IACUC-2023-0111).

Statistical Analysis

Data analysis was performed using OriginPro 2018C (OriginLab) and Fiji-ImageJ (NIH, USA). All quantitative data were analyzed using GraphPad Prism 9.0 and are expressed as mean ± standard deviation (SD). Statistical comparisons between two groups were performed using unpaired two-tailed Student's *t*-test, while one-way or two-way ANOVA was used for multiple group comparisons, followed by Dunnett's or Tukey's post hoc tests as appropriate. Survival analysis was conducted using the Log rank test, and univariate and multivariate Cox proportional hazards models were applied to assess independent prognostic factors. P values less than 0.05 were considered statistically significant (NS: not significant, *P < 0.05, **P < 0.01, ***P < 0.001, ****P < 0.0001).

Results

Expression and Prognostic Significance of PSMA (*FOLH1*) in PCa

We utilized the TIMER database to analyze the expression of PSMA (Encoded by *FOLH1*) in different cancerous and normal tissues. The results revealed that PSMA expression is significantly upregulated in certain cancers. Notably, PSMA expression in Prostate Adenocarcinoma (PRAD) far exceeds its levels in other tumor tissues, highlighting its potential significance (Figure 1a). Using the Prostate Cancer Atlas database, pseudotime analysis was performed to map the progression of PCa from normal tissue (n=167) to primary tumors (n=499), then to androgen receptor-positive prostate cancer (ARPC, n=418), neuroendocrine PCa (NEPC, n=34), and ultimately to double-negative PCa (DNPC, n=22) (Figure 1b). Quantitative analysis revealed a significant upregulation of PSMA expression in the early stages (Primary tumors and ARPC) of PCa, followed by a gradual decline as the disease progresses to NEPC and DNPC (Figure 1c), which is similar to the progression trajectory of PCa. This intriguing pattern suggests that PSMA could serve as a crucial marker for early diagnosis and therapeutic intervention in PCa (Figure 1c). To further validate the expression levels of PSMA, cancerous and adjacent normal tissues from three clinical patients (n=3 per group) were collected. Although only three patient samples were analyzed by IHC, all exhibited strong PSMA expression in tumor tissues compared to adjacent normal tissues, consistent with the public database results. Due to the limited sample size, no statistical analysis was performed on the IHC data, and these results serve as qualitative validation rather than independent statistical confirmation. Comprehensive assessments through HE and IHC confirmed significantly higher PSMA expression in tumor tissues compared to normal tissues (Figure 1d and e). Lastly, Kaplan-Meier survival analysis with patients stratified by PSMA expression (based on the best-cut-off value) revealed a trend toward lower OS and DFS in the high PSMA expression group. Specifically, DFS was significantly lower in the high-expression group compared to the low-expression group (P = 0.00034, Figure 1f and g). Univariate Cox regression analysis demonstrated that high PSMA expression was significantly associated with worse DFS (BCR-free survival), with a hazard ratio (HR) of 2.41 (95% CI: 1.46–3.95, P = 0.001, Figure 1h and i). However, after adjusting for age, Gleason score, pathological T stage, and N stage in multivariate Cox regression analysis, the association between PSMA expression and DFS was no longer statistically significant (P = 0.070, Figure 1h and i). These results suggest that while PSMA expression may have prognostic value, it is not an independent influencing factor for DFS when other clinical variables are considered.

Expression of PSMA (*FOLH1*) in Different Clinical Subgroups

To investigate the relationship between PSMA expression and clinical characteristics of PCa, we analyzed datasets from the UALCAN database across various clinical subgroups. PSMA expression was significantly higher in T1-T3 stages compared to normal tissues, but no significant differences were observed among the T stages (Supplementary Figure 1a). In contrast, expression levels in PCa patients across different ethnic groups were consistently and significantly higher than in normal individuals (Supplementary Figure 1b). Notably, patients with metastases exhibited significantly elevated PSMA expression compared to those normal (Supplementary Figure 1c). In relation to Gleason scores, PSMA levels demonstrated an increasing trend with higher scores, but at a Gleason score as high as 10, PSMA expression shows no statistically significant difference compared to that in normal controls (Supplementary Figure 1d), which reflects similarities with the trend of low PSMA expression in NEPC and DNPC (Figure 1b and 1c). Analysis of molecular subtypes revealed that PSMA was generally overexpressed across most subtypes (*ERG*-fusion, *ETV1*-fusion, *ETV4*-fusion, *FOXA1*-mutation, and *SPOP*-mutation subtypes), with the exception of the *FLI*-fusion and *IDH1*-mutation subtypes, where expression levels were similar to those of normal tissue (Supplementary Figure 1e). Additionally, a relationship between *TP53* mutations and PSMA expression was identified, indicating potential relevance in PCa progression (Supplementary Figure 1f). These findings suggest that PSMA expression correlates with clinical features such as age, metastatic status, Gleason score, and molecular subtypes, highlighting its potential as a biomarker for diagnosis and prognosis in PCa.

https://doi.org/10.2147/IJN.S532080

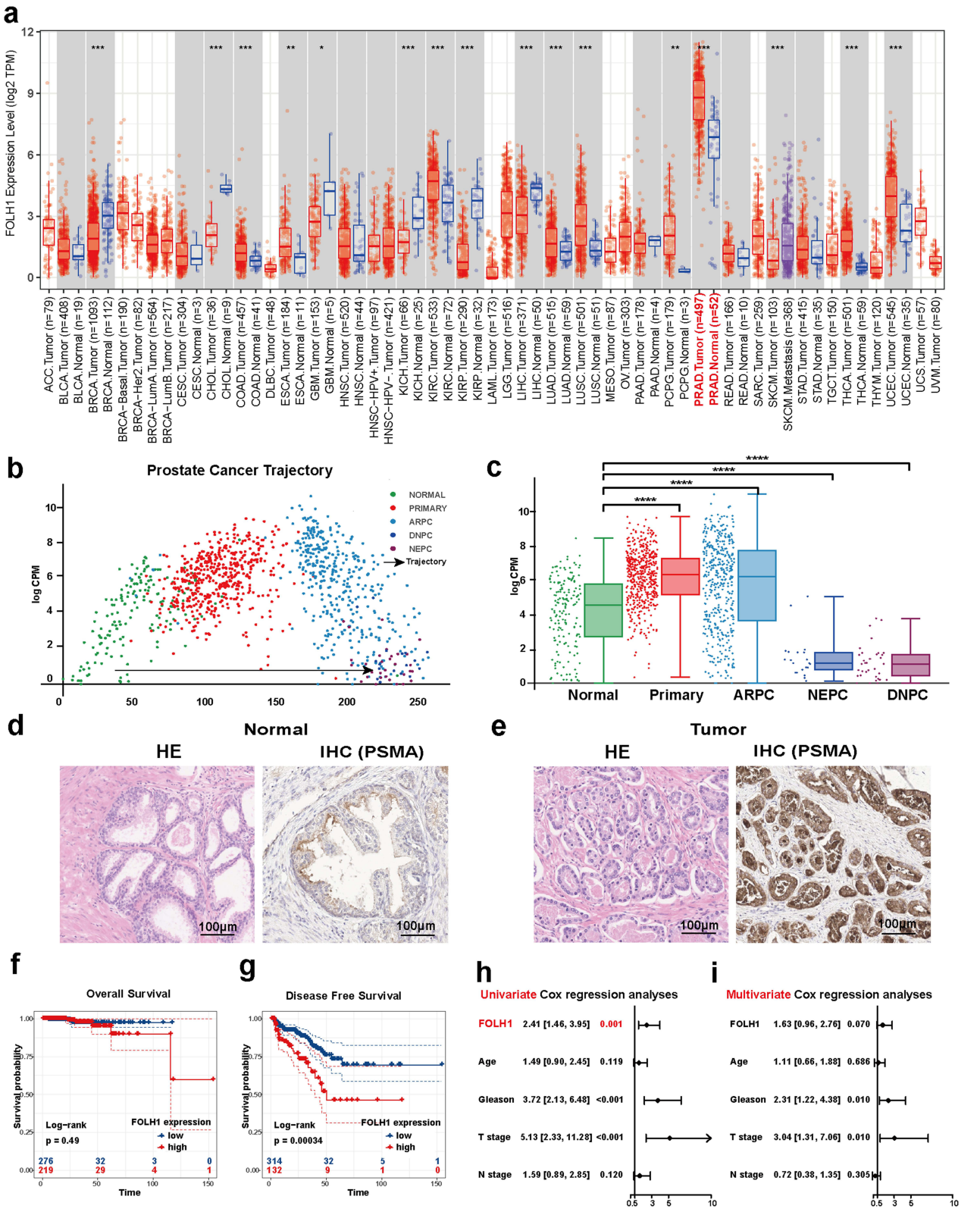

Figure 1 Expression profile and prognostic significance of PSMA (*FOLH1*) in prostate cancer. (**a**) PSMA expression across 33 cancer types, as analyzed from the TIMER database (Student's *t*-test). (**b**) Pseudotime trajectory of prostate cancer progression constructed from transcriptomic profiles in the Prostate Cancer Atlas. (**c**) PSMA expression levels in normal prostate tissue (n = 167), primary prostate cancer (n = 499), androgen receptor-positive prostate cancer (ARPC, n = 418), neuroendocrine prostate cancer (NEPC, n = 34), and double-negative prostate cancer (DNPC, n = 22), with comparisons to the normal group (one-way ANOVA with Dunnett's post hoc test). (**d** and **e**) Representative HE and PSMA IHC staining of matched normal and tumor tissues (n = 3). (**f** and **g**) Kaplan–Meier survival analysis showing overall survival (OS) and disease-free survival (DFS) in patients stratified by PSMA expression levels (Log rank test). (**h** and **i**) Univariate and multivariate Cox regression analyses identifying PSMA expression as an independent prognostic factor in prostate cancer (Cox proportional hazards model). *P < 0.05, **P < 0.01, ***P < 0.001, ****P < 0.0001. Scale bar: 100 μm.

Synthesis and Construction of the PSMA-Targeted Probe and Basic Optical Characterization

Based on the findings above, PSMA has been identified as a viable molecular target for specific diagnostic and therapeutic applications. We developed a PSMA-targeted probe using the previously reported NIR material OSP_{12} NPs.[29] The probe was constructed by self-assembling OSP_{12} with DSPE-PEG-Mal to form nanoparticles, which were subsequently conjugated to the PSMA-targeting ligand ACUPA via thiol–maleimide coupling, resulting in the formation of the specific PSMA-targeted probe, PSMA-OSP_{12} NPs (Figure 2a). The optical properties of PSMA-OSP_{12} NPs, analyzed through spectral analysis, revealed that the probe exhibits excitation at 792.0 nm and emission at 1049.0 nm, extending its tail to approximately 1500 nm. This demonstrates the imaging capability of PSMA-OSP_{12} NPs in the NIR-II region (Figure 2b). We used 100 μg/mL of ACUPA-SH, OSP_{12} NPs, and PSMA-OSP_{12} NPs under 1000 LP and 100 ms exposure conditions. ACUPA-SH exhibited negligible fluorescence signal, while the other two groups showed comparable fluorescence intensities (Figure 2c and d). Dynamic light scattering (DLS) analysis revealed that the hydrodynamic diameter of the PSMA-OSP_{12} NPs was 66.61 ± 21.10 nm, with a polydispersity index (PDI) of 0.100, indicating a moderately uniform size distribution. In contrast, the non-targeted OSP_{12} NPs showed a smaller average diameter of 59.53 ± 18.30 nm and a lower PDI of 0.094, confirming that the conjugation of the PSMA-targeting ligand ACUPA modestly increased particle size and dispersity (Supplementary Figure 2a and b).

Based on the feed molar ratio (ACUPA-SH: DSPE-PEG-Ma ≈ 1.25:1), the average PEG-lipid surface density (~1000–1500 chains per nanoparticle), and a reported thiol–maleimide conjugation efficiency of approximately 60%,[35] we estimate that each PSMA-OSP_{12} NPs carries approximately 600–900 ACUPA molecules on its surface.

To evaluate photostability, both formulations were incubated in PBS at 4 °C and monitored for fluorescence intensity at Days 0, 3, and 7. As shown in Supplementary Figure 3a and b, the fluorescence signals of OSP_{12} NPs and PSMA-OSP_{12} NPs remained stable over the 7-day observation period. At Day 3, OSP12 NPs retained $89.24 \pm 3.92\%$ of their initial signal, while PSMA-OSP_{12} NPs maintained $85.06 \pm 2.20\%$. By Day 7, fluorescence retention was $74.50 \pm 2.42\%$ for OSP_{12} NPs and $71.42 \pm 2.35\%$ for PSMA-OSP_{12} NPs, respectively. These results confirm that the surface modification with ACUPA does not impair the inherent photostability of the OSP_{12} NPs fluorophore and support its suitability for prolonged in vivo imaging.

Additionally, PSMA-OSP_{12} NPs achieved high-definition imaging up to 1300 nm in the NIR-II region in vitro and in vivo (Figure 2e and f) and the fluorescence intensity of PSMA-OSP_{12} NPs increased with its concentration (Figure 2g). In vivo imaging, the PSMA-OSP_{12} NPs (1 mg/mL) achieved clear imaging under an 1100 nm filter, with a relatively strong fluorescence intensity ($P < 0.0001$, Figure 2h) and a higher TBR of 7.61 ± 0.19, which was significantly higher than that of other groups ($P < 0.0001$, Figure 2i).

In vitro Validation of PSMA-Specific Binding of PSMA-OSP_{12} NPs

To select an appropriate cell line for xenograft tumor modeling, PSMA expression levels were first evaluated in five human prostate cell lines using flow cytometry (Supplementary Figure 4a). LNCaP and VCaP exhibited nearly 100% PSMA positivity, while 22Rv1 showed moderate-to-high expression levels (60–70%). In contrast, PSMA expression was low in PC-3 and RWPE-1 cells (2–4%). Although LNCaP cells exhibit high PSMA expression, their poor tumorigenic capacity in BALB/c nude mice has been widely reported in the literature[36] and was further validated by our preliminary in vivo experiments. Additionally, VCaP and RWPE-1 are rarely used for subcutaneous xenograft modeling due to their limited in vivo growth potential. Considering both PSMA expression and tumorigenicity, 22Rv1 cells were selected for subsequent xenograft model establishment (Supplementary Figure 4b). PC-3 cells, which lack PSMA expression, were used as the negative control cell line.[37]

Based on the differential PSMA expression profiles observed in prostate cancer cell lines, we next evaluated the PSMA-targeting capability of PSMA-OSP_{12} NPs using PSMA-positive 22Rv1 cells and PSMA-negative PC-3 cells. In vitro NIR-II fluorescence imaging was performed under four treatment conditions (Figure 3a).

In Control 1 (PC-3 + PSMA-OSP_{12} NPs), PSMA-negative PC-3 cells exhibited minimal fluorescence, indicating negligible nonspecific binding. In Control 2 (22Rv1 + free OSP_{12} NPs), 22Rv1 cells showed weak fluorescence when

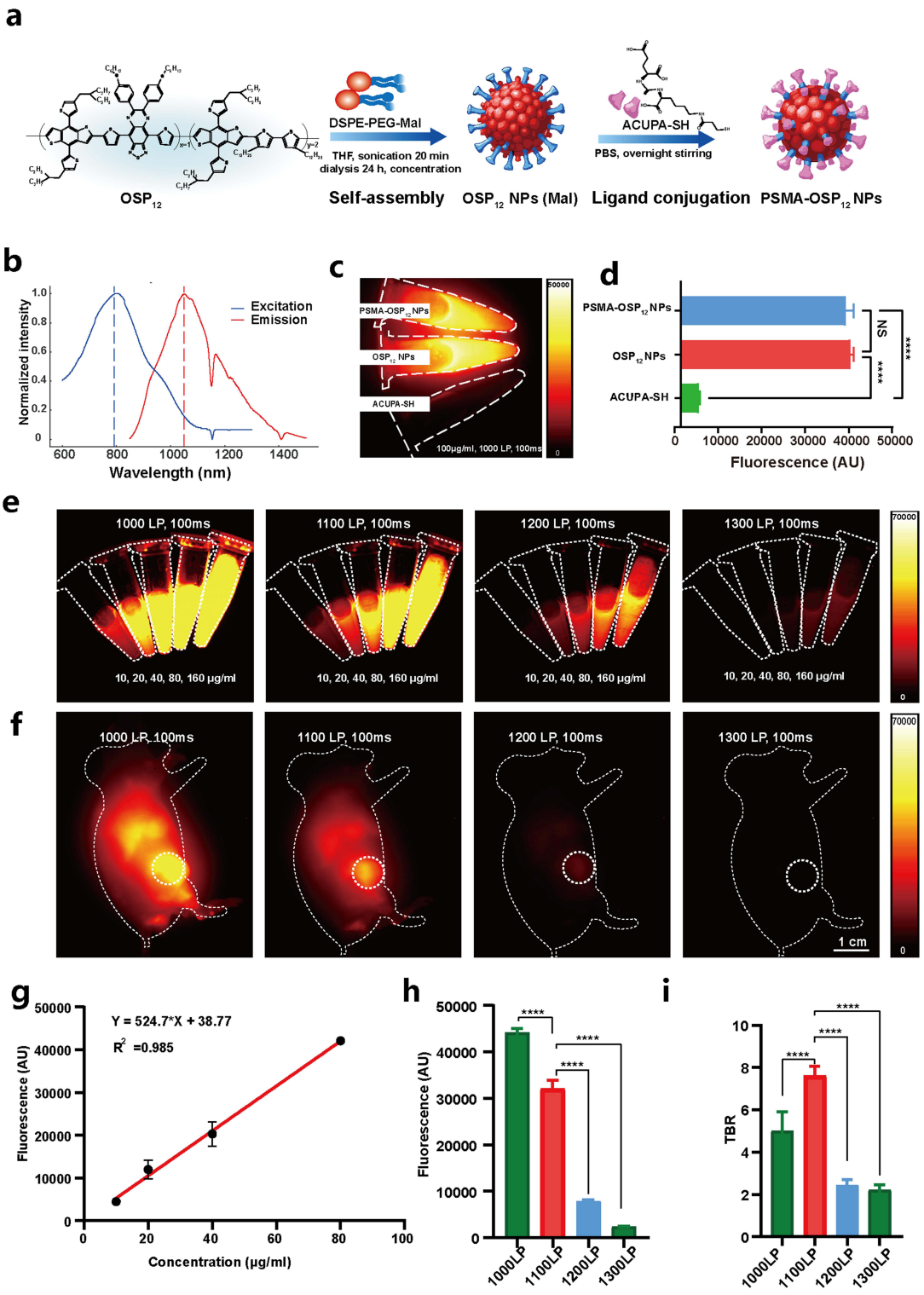

Figure 2 Synthesis, optical characterization, and imaging performance of PSMA-OSP$_{12}$ NPs. (**a**) Schematic illustration of PSMA-OSP$_{12}$ NPs synthesis. OSP$_{12}$ self-assembles with DSPE-PEG-Mal to form micelles with maleimide terminals, which are conjugated to ACUPA-SH via thiol–maleimide chemistry. (**b**) Excitation (blue) and emission (red) spectra of PSMA-OSP$_{12}$, showing NIR-II fluorescence characteristics. (**c**) Comparative fluorescence imaging of ACUPA-SH, OSP$_{12}$ NPs, and PSMA-OSP$_{12}$ NPs under identical conditions (100 μg/mL; 1000 nm LP filter). (**d**) Quantification of fluorescence intensities from (**c**) (one-way ANOVA). (**e**) In vitro fluorescence imaging of PSMA-OSP$_{12}$ NPs at serial concentrations (10–160 μg/mL) under different long-pass (LP) filters (1000–1300 nm). (**f**) In vivo fluorescence imaging of tumor-bearing mice injected with PSMA-OSP$_{12}$ NPs under the same LP filters and exposure conditions. (**g**) Linear relationship between fluorescence intensity and probe concentration (R^2 = 0.997). (**h**) Quantified fluorescence intensity of tumors under different LP filters (one-way ANOVA vs 1100 nm LP). (**i**) Tumor-to-background ratio (TBR) under varying LP filters showing maximum imaging contrast at 1100 nm (one-way ANOVA). All imaging was performed using a laser power of 60 mW/cm² and an exposure time of 100 ms. ****P < 0.0001, 1 cm.

Abbreviation: NS, not significant.

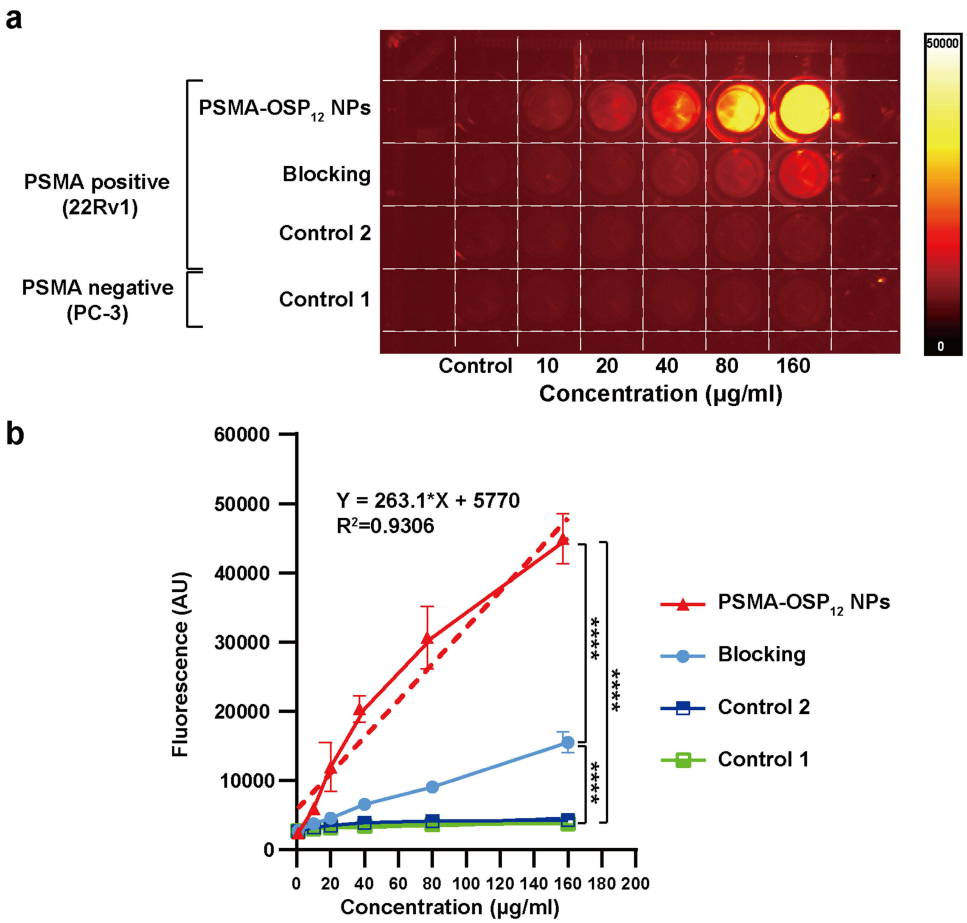

Figure 3 In vitro binding specificity and blocking validation of PSMA-OSP_{12} NPs. (**a**) Fluorescence imaging of PSMA-positive 22Rv1 and PSMA-negative PC-3 cells under four treatment conditions: control 1, PSMA-negative PC-3 cells incubated with PSMA-OSP_{12} NPs; control 2, 22Rv1 cells incubated with free OSP_{12} NPs (non-targeted); blocking group, 22Rv1 cells pretreated with ACUPA-SH (10 μM, 1 h) prior to PSMA-OSP_{12} NPs exposure; and experimental group, 22Rv1 cells directly incubated with PSMA-OSP_{12} NPs (10–160 μg/mL, 24 h). (**b**) Quantification of fluorescence intensities revealed a significant, concentration-dependent increase in the experimental group. In contrast, control 1 (PC-3 + PSMA-OSP_{12} NPs) and control 2 (22Rv1 + free OSP_{12} NPs) showed no significant difference and maintained low signal levels. Blocking with ACUPA-SH markedly reduced fluorescence intensity, confirming the PSMA-specific binding of PSMA-OSP_{12} NPs (two-way ANOVA). (n = 3 per group). ****P < 0.0001.

incubated with non-targeted OSP_{12} NPs, confirming the absence of passive uptake. In the blocking group (22Rv1 pretreated with ACUPA-SH before PSMA-OSP_{12} incubation), fluorescence signals were significantly suppressed across all concentrations, suggesting effective competitive inhibition of PSMA binding by free ligand. By contrast, the experimental group (22Rv1 + PSMA-OSP_{12} NPs) exhibited a concentration-dependent increase in fluorescence intensity. Quantitative analysis (Figure 3b) demonstrated a strong linear correlation between probe concentration and signal intensity ($Y = 263.1*X + 5770$, $R^2 = 0.9306$), validating dose-dependent, receptor-mediated cellular uptake. These results confirm the high specificity of PSMA-OSP_{12} toward PSMA-expressing tumor cells, highlighting its potential for quantitative molecular imaging applications.

Specific Tumor Targeting and Biodistribution Profile of PSMA-OSP_{12} NPs

To comprehensively evaluate the in vivo tumor-targeting capability and biodistribution of PSMA-OSP_{12} NPs, we established a human-derived 22Rv1 xenograft mouse model and compared three treatment groups: control (OSP_{12} NPs), blocking (ACUPA pre-injection + PSMA-OSP_{12} NPs), and experimental (PSMA-OSP_{12} NPs).

In the control group, non-targeted OSP_{12} NPs exhibited rapid hepatic accumulation with minimal tumor signal, which gradually decreased over time due to metabolic clearance. The blocking group, pretreated with ACUPA (10 mM, 1 h prior to probe administration), also showed limited tumor fluorescence, highlighting the successful inhibition of PSMA receptor binding (Figure 4a). In contrast, mice in the experimental group receiving PSMA-OSP_{12} NPs demonstrated

https://doi.org/10.2147/IJN.S532080

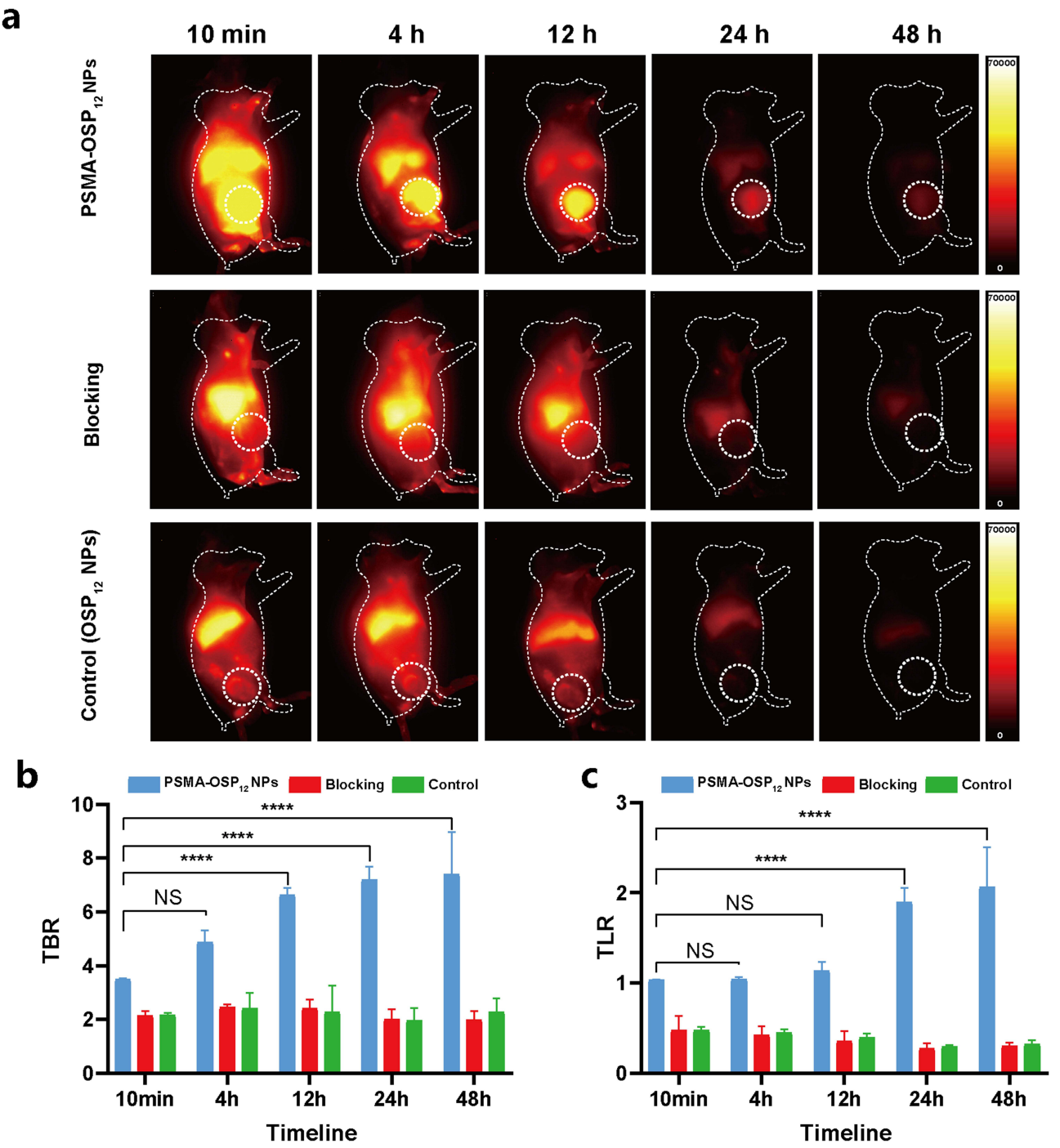

Figure 4 In vivo tumor targeting and biodistribution of PSMA-OSP_{12} NPs. (**a**) Representative NIR-II fluorescence images of 22Rv1 xenograft-bearing mice at multiple time points following intravenous injection of non-targeted OSP_{12} NPs (control group), PSMA-OSP_{12} NPs with ACUPA pre-blocking (blocking group), or PSMA-OSP_{12} NPs (experimental group). Imaging was performed under identical parameters (808 nm excitation, 1100 nm long-pass filter, 100 ms exposure). (**b** and **c**) Quantitative analysis of tumor-to-background ratio (TBR) and tumor-to-liver ratio (TLR) demonstrates significantly higher tumor accumulation and specificity in the PSMA-OSP_{12} NPs group relative to both control and blocking groups (two-way ANOVA) and Post hoc power analysis. ****P < 0.0001.
Abbreviation: NS, not significant.

evident tumor localization beginning at 4 h post-injection, with fluorescence intensities progressively intensifying and peaking between 24–48 h. Quantitative analysis revealed significantly higher TBR in the experimental group compared to both control and blocking groups, with values reaching 7.19 ± 0.40 and 7.40 ± 1.28 at 24 h and 48 h, respectively (Figure 4b). TLR analysis similarly demonstrated enhanced tumor specificity, with liver signal gradually declining post-

injection (Figure 4c). These findings confirm the selective in vivo binding of PSMA-OSP_{12} NPs to PSMA-expressing tumors and the efficacy of ACUPA-mediated blocking in suppressing this interaction.

To further characterize tissue-level distribution, ex vivo imaging at 48 h post-injection revealed that PSMA-OSP_{12} NPs predominantly accumulated in tumors, liver, and kidneys, whereas non-targeted OSP_{12} NPs and the blocking group showed minimal tumor retention and increased hepatic uptake (Supplementary Figure 5a). Quantitative organ fluorescence analysis confirmed significantly elevated tumor signal in the PSMA-OSP_{12} NPs group (Supplementary Figure 5b, $P < 0.0001$). HE and PSMA IHC validated tumor identity and confirmed PSMA positivity across all groups (Supplementary Figure 5c), ruling out differential antigen expression as a source of imaging discrepancy.

Excretion profiling further indicated that PSMA-OSP_{12} NPs are primarily cleared via the hepatobiliary pathway. Serial NIR-II imaging of feces and urine collected daily up to 5 days post-injection revealed robust fluorescence signals in feces but negligible signal in urine, confirming predominant fecal elimination with minimal renal involvement (Supplementary Figure 6).

These collective results highlight the high tumor specificity, favorable biodistribution, and safe excretion profile of PSMA-OSP_{12} NPs, underscoring its potential utility for NIR-II fluorescence-guided cancer imaging.

Tumor-Specific Visualization of ex vivo Tumor Tissues Using the PSMA-OSP_{12} NPs Probe as a Molecular-Level Pathological Imaging Tool

To explore the applicability of PSMA-OSP_{12} NPs for ex vivo tumor margin visualization, we employed a 22Rv1 xenograft prostate cancer model and conducted NIR-II fluorescence imaging of excised tumor sections. Following tumor resection, samples were sectioned into ~2 mm-thick slices, blocked with 5% FBS, incubated with 200 μg/mL of either PSMA-OSP_{12} NPs or OSP_{12} NPs (control), and washed thoroughly with PBS prior to imaging (Figure 5a).

As shown in Figure 5b, tumor slices incubated with PSMA-OSP_{12} NPs exhibited robust fluorescence localized within tumor boundaries, indicative of specific probe-target interaction. In contrast, tumor slices incubated with non-targeted OSP_{12} NPs showed weak fluorescence, which was largely eliminated during washing, suggesting limited retention due to nonspecific interactions. Fluorescence intensity profile analysis (Figure 5c) revealed that signal distribution in the PSMA-OSP_{12} NPs group was substantially higher and well-defined relative to the control group.

Quantitative analysis confirmed a significantly enhanced fluorescence signal in the PSMA-OSP_{12} NPs group compared to the OSP_{12} NPs group ($P < 0.0001$, Figure 5d). These results demonstrate the capability of PSMA-OSP_{12} NPs to achieve highly specific tumor labeling in tissue slices, underscoring its potential utility as a molecular-level pathological imaging tool for intraoperative guidance or ex vivo diagnostic applications.

Biosafety Evaluation of PSMA-OSP_{12} NPs

To evaluate the in vivo biosafety profile of PSMA-OSP_{12} NPs, a comprehensive toxicity assessment was performed in healthy mice over a 14-day period. Throughout the study, no significant changes in body weight or general health status were observed in mice treated with PSMA-OSP_{12} NPs compared to those receiving PBS (Figure 6a), suggesting minimal systemic toxicity. To further assess hematological safety, blood samples were collected on days 0, 7, and 14 post-injection. Analysis of hematological parameters—including RBC, WBC, PLT—revealed no significant differences between the PSMA-OSP_{12} NPs and PBS control groups (Figure 6b–d). These findings indicate that administration of PSMA-OSP_{12} NPs does not disrupt normal hematopoiesis or immune homeostasis. In addition, serum biochemical indices related to liver and kidney function were examined. Key markers—ALT, AST, ALB, BUN, and CREA—remained within physiological ranges in both groups, with no significant alterations detected at any time point (Figure 6e–i), indicating no measurable hepatic or renal toxicity. At the end of the study (day 14), major organs (heart, liver, spleen, lung, and kidney) were harvested for histopathological evaluation. HE staining revealed no pathological abnormalities or tissue damage in the PSMA-OSP_{12} NPs group compared to PBS controls (Figure 6j). Collectively, these results demonstrate that PSMA-OSP_{12} NPs possess an excellent biocompatibility and safety profile, with no evidence of systemic, hematologic, or organ-specific toxicity under the tested conditions.

https://doi.org/10.2147/IJN.S532080

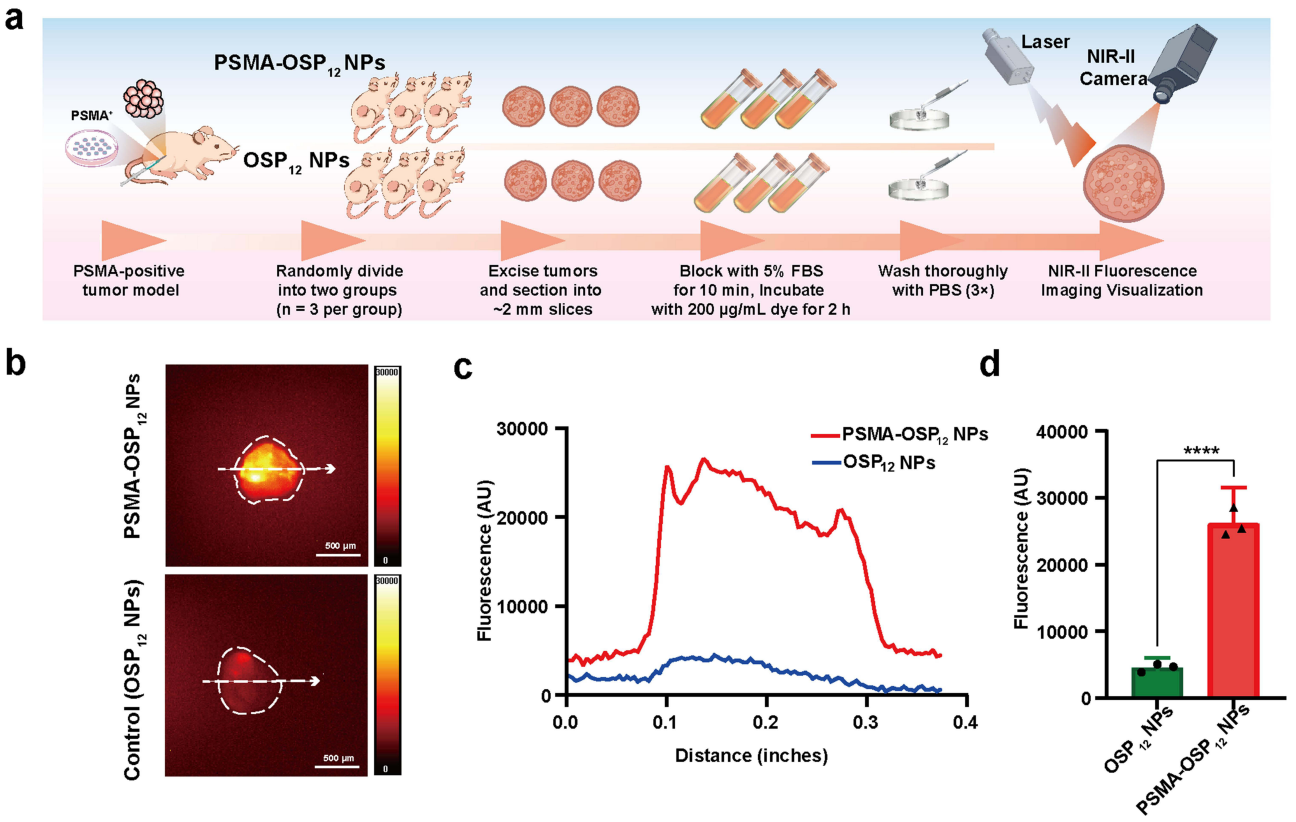

Figure 5 Ex vivo tumor-specific visualization using PSMA-OSP_{12} NPs. (**a**) Schematic diagram of the ex vivo NIR-II imaging workflow. Tumor-bearing mice (22Rv1 xenografts, n = 6) were randomly divided into two groups (n = 3 per group). Excised tumors were sectioned into ~2 mm slices, blocked with 5% FBS for 10 min, then incubated with either OSP_{12} NPs (control group) or PSMA-OSP_{12} NPs (experimental group) at 200 μg/mL for 2 h at room temperature, followed by three PBS washes. Imaging was performed using an NIR-II system (808 nm laser, 1100 nm long-pass filter, 100 ms exposure). (**b** and **c**) Representative fluorescence images and corresponding intensity profiles of tumor slices showed markedly stronger signal in the PSMA-OSP_{12} NPs group. (**d**) Quantification of fluorescence intensity confirmed significantly enhanced tumor labeling in the PSMA-OSP_{12} NPs group compared to control (Student's *t*-test, ****P < 0.0001). Scale bar, 500 μm.

Discussion

PSMA has long been recognized as a valuable biomarker for PCa and other cancers diagnosis and therapy.[2,10,38–42] In this study, we extended the current understanding by leveraging large-scale datasets and pseudotime trajectory analysis to reveal dynamic patterns of PSMA expression across PCa subtypes. Our data confirmed the elevated expression of PSMA in early-stage PCa, which gradually declines in aggressive subtypes such as NEPC and DNPC (Figure 1). This decline may be attributed to androgen receptor (AR) pathway suppression and the prevalence of TP53 mutations, which promote dedifferentiation and lineage plasticity.[31,43–45] These results highlight the biological significance of PSMA as a biomarker and provide a compelling rationale for its application in molecular imaging.

Despite the clinical availability of PSMA-targeted radioligands, including ^{68}Ga-PSMA-11 and ^{177}Lu-PSMA-617, their reliance on radiation limits their use in real-time surgical navigation and intraoperative decision-making.[46–49] Moreover, their molecular structures hinder integration into nanoprobe platforms due to hydrophobicity, lack of reactive groups, or bulky chelators.[10,50,51] In contrast, ACUPA-SH, used in this study, retains high binding affinity and incorporates a thiol group, enabling site-specific conjugation via maleimide-thiol chemistry. This bioconjugation approach offers several advantages: it proceeds under mild aqueous conditions, forms stable covalent thioether bonds, and minimizes nonspecific interactions, ensuring consistent batch-to-batch reproducibility.[11,12,52] The resulting PSMA-OSP_{12} NPs thus achieve precise ligand orientation, enhanced stability, and reliable performance in vivo.

To overcome the limitations of NIR-I dyes such as S0456 (used in OTL78; excitation/emission: 774–776/794–796 nm) and Cy7 (used in Cy-KUE-OA; emission at 776 nm), which suffer from shallow tissue penetration and high background autofluorescence, we selected OSP_{12} as the fluorophore for our nanoprobe.[27,28,53,54] PSMA-OSP_{12} NPs exhibits excitation

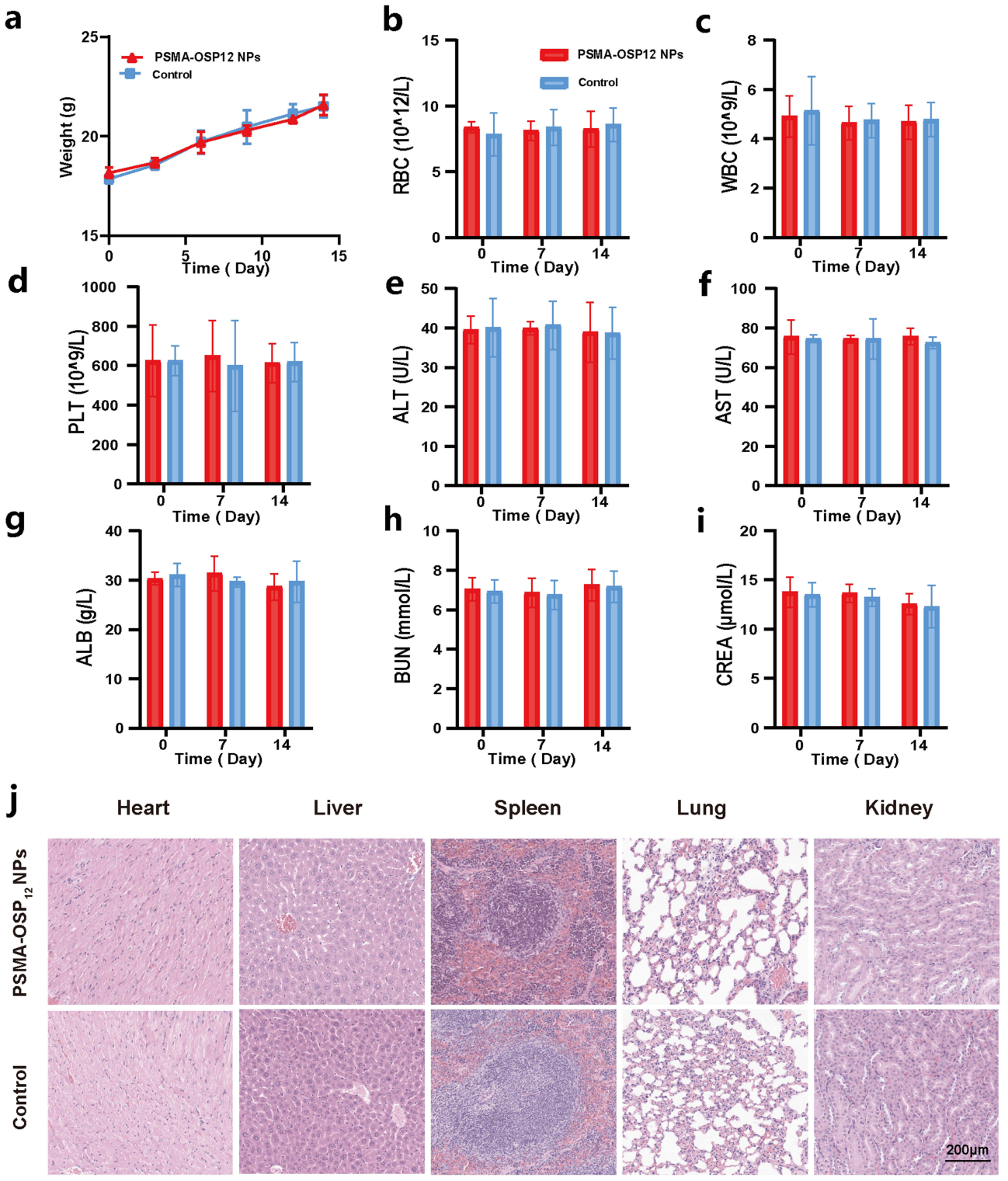

Figure 6 Biosafety evaluation of PSMA-OSP$_{12}$ NPs. (**a**) Body weight monitoring of mice treated with PSMA-OSP$_{12}$ NPs or PBS over a 14-day period showed no significant differences. (**b**–**d**) Hematological parameters, including red blood cell (RBC) count, white blood cell (WBC) count, and platelet (PLT) count, remained within normal ranges in both groups. (**e**–**i**) Serum biochemical markers related to liver and kidney function, including alanine aminotransferase (ALT), aspartate aminotransferase (AST), albumin (ALB), blood urea nitrogen (BUN), and creatinine (CREA), showed no significant abnormalities in the PSMA-OSP$_{12}$ NP group compared to controls. (**j**) Representative hematoxylin and eosin (HE) staining of major organs (heart, liver, spleen, lung, kidney) revealed no visible pathological lesions in either group. No statistically significant differences were observed across all parameters (n=5 per group, two-way ANOVA). Scale bar, 200 μm.

https://doi.org/10.2147/IJN.S532080

at 792.0 nm and emission at 1049.0 nm, placing it firmly in the NIR-II window.[29] Compared with clinically available dyes, OSP_{12} offers superior photostability, deeper tissue penetration, reduced scattering, and negligible autofluorescence. These optical advantages enabled PSMA-OSP_{12} NPs to achieve a TBR of 7.40 ± 1.28 at 48 hours post-injection, significantly outperforming OTL-78 (TBR ~2.0) and Cy-KUE-OA (TBR ~3.8).[28,53] Recent advances such as FC-PSMA have demonstrated the feasibility of PSMA-targeted NIR-II imaging in preclinical models, but suffer from drawbacks including complex synthesis routes, suboptimal in vivo stability, or limited modularity.[34,55] In contrast, our strategy offers a more practical and translational pathway while maintaining excellent imaging performance. This extended imaging window supports flexible scheduling of fluorescence-guided surgery (FGS) and enhances tumor delineation even under standard surgical lighting conditions. Notably, the deeper tissue penetration (>1 cm) and high SBR of NIR-II imaging overcome the resolution limitations of traditional NIR-I agents and support real-time intraoperative use.

Beyond in vivo applications, PSMA-OSP_{12} NPs demonstrated substantial utility in ex vivo settings. Rapid incubation of freshly resected PCa specimens allowed for high-contrast visualization of tumor margins without the need for systemic administration. This approach avoids individual variability in pharmacokinetics and seamlessly integrates with conventional pathological workflows.[56] While ex vivo fluorescence imaging has been explored in other malignancies such as lung and colorectal cancers, our study represents the first application of a NIR-II PSMA-targeted probe in prostate cancer.[23,24,57] This capability offers a novel solution for intraoperative margin assessment and immediate postoperative diagnostics.

Ensuring biosafety is essential for clinical translation. In this study, we conducted comprehensive toxicity evaluations, including body weight monitoring, hematological and biochemical analyses, and histopathological examinations. The results revealed no significant adverse effects in major organs, and PSMA-OSP_{12} NPs were predominantly cleared via hepatobiliary excretion, minimizing the risk of long-term retention. These findings align with previous NIR-II nanoprobe safety studies and support the translational potential of PSMA-OSP_{12} NPs.[18]

While our findings underscore the promise of PSMA-OSP_{12} NPs, several translational challenges must be addressed. Current imaging systems are not universally compatible with NIR-II wavelengths, necessitating the development of affordable and user-friendly detection platforms such as fiber-optic or laparoscopic modules.[58,59] Additionally, the cost of producing high-quality NIR-II fluorophores remains substantial, although improved clinical outcomes may justify these investments.[17] Finally, given the heterogeneity of PSMA expression, patient selection strategies and imaging-guided treatment algorithms will be essential for maximizing benefit. Importantly, NIR-II imaging is not intended to replace PET or other modalities, but rather to serve as a complementary tool offering superior spatial resolution and intraoperative utility.

Conclusions

In summary, this study presents PSMA-OSP_{12} NPs as a novel NIR-II nanoprobe with high specificity for PSMA-positive prostate cancer. By integrating the favorable binding characteristics of ACUPA-SH, the optical advantages of OSP_{12}, and a stable maleimide-thiol conjugation strategy, we successfully constructed a nanoprobe with outstanding tumor-targeting ability, high spatial resolution, and deep tissue penetration. The probe demonstrates excellent performance both in vivo and ex vivo, and exhibits favorable biosafety, indicating its translational potential. Although further studies are required to optimize clinical integration, PSMA-OSP_{12} NPs offer a promising platform for real-time fluorescence-guided surgery and rapid pathological assessment, representing an important step forward in the development of precision diagnostics for prostate cancer.

Data Sharing Statement

Data from public databases can be accessed at the following websites: TIMER: http://timer.cistrome.org/; Prostate Cancer Atlas: https://prostatecanceratlas.org/; GEPIA: http://gepia.cancer-pku.cn/index.html. All study materials are included within the manuscript. The original contributions presented in this study are included in the article/supplementary material. Further inquiries can be directed to the corresponding author.

Ethics Declarations

The study was conducted in accordance with the Declaration of Helsinki, and approved by the Ethics Committee of the Ethics Committee of Shenzhen Hospital, Chinese Academy of Medical Sciences (JS2024-7-1). Informed consent was obtained from all subjects involved in the study. Written informed consent has been obtained from the patient to publish this paper.

Author Contributions

All authors made a significant contribution to the work reported, whether that is in the conception, study design, execution, acquisition of data, analysis and interpretation, or in all these areas; took part in drafting, revising or critically reviewing the article; gave final approval of the version to be published; have agreed on the journal to which the article has been submitted; and agree to be accountable for all aspects of the work.

Funding

This work was supported by National Cancer Center/National Clinical Research Center for Cancer/Cancer Hospital & Shenzhen Hospital, Chinese Academy of Medical Sciences and Peking Union Medical College Institutional Research Project Funding (NO. SZ2020ZD003), and Sanming Project of Medicine in Shenzhen (NO. SZSM202111003).

Disclosure

The authors declare no conflicts of interest.

References

1. James ND, Tannock I, N'Dow J, et al. The Lancet Commission on prostate cancer: planning for the surge in cases. *Lancet*. 2024;403 (10437):1683–1722. doi:10.1016/S0140-6736(24)00651-2
2. Jiang Z, Kadeerhan G, Zhang J, Guo W, Guo H, Wang D. Advances in prostate-specific membrane antigen-targeted theranostics: from radionuclides to near-infrared fluorescence technology. *Front Immunol*. 2025;15.
3. Sailer V, von Amsberg G, Duensing S, et al. Experimental in vitro, ex vivo and in vivo models in prostate cancer research. *Nat Rev Urol*. 2023;20 (3):158–178. doi:10.1038/s41585-022-00677-z
4. Bray F, Laversanne M, Sung H, et al. Global cancer statistics 2022: GLOBOCAN estimates of incidence and mortality worldwide for 36 cancers in 185 countries. *CA*. 2024;74(3):229–263. doi:10.3322/caac.21834
5. Siegel RL, Giaquinto AN, Jemal A. Cancer statistics, 2024. *CA*. 2024;74(1):12–49. doi:10.3322/caac.21820
6. Kadeerhan G, Xue B, Wu XL, Chen WN, Wang DW. Incidence trends and survival of metastatic prostate cancer with bone and visceral involvement: 2010-2019 surveillance, epidemiology, and end results. *Front Oncol*. 2023;13:1201753. doi:10.3389/fonc.2023.1201753
7. Horoszewicz JS, Kawinski E, Murphy GP. Monoclonal antibodies to a new antigenic marker in epithelial prostatic cells and serum of prostatic cancer patients. *Anticancer Res*. 1987;7(5b):927–935.
8. Hennrich U, Eder M. [(68)Ga]Ga-PSMA-11: the First FDA-Approved (68)Ga-radiopharmaceutical for PET imaging of prostate cancer. *Pharmaceuticals*. 2021;14(8):713. doi:10.3390/ph14080713
9. Hennrich U, Eder M. [(177)Lu]Lu-PSMA-617 (Pluvicto(TM)): the first FDA-approved radiotherapeutical for treatment of prostate cancer. *Pharmaceuticals*. 2022;15(10):1292. doi:10.3390/ph15101292
10. Jiao J, Zhang J, Wen W, Qin W, Chen X. Prostate-specific membrane antigen-targeted surgery in prostate cancer: accurate identification, real-time diagnosis, and precise resection. *Theranostics*. 2024;14(7):2736–2756. doi:10.7150/thno.95039
11. Meher N, Ashley GW, Bidkar AP, et al. Prostate-specific membrane antigen targeted deep tumor penetration of polymer nanocarriers. *ACS Appl Mater Interfaces*. 2022;14(45):50569–50582. doi:10.1021/acsami.2c15095
12. Jana D, Han Z, Huang X, et al. Enhanced prostate-specific membrane antigen targeting by precision control of DNA scaffolded nanoparticle ligand presentation. *ACS nano*. 2024;18(26):16674–16683. doi:10.1021/acsnano.4c01640
13. Bednova O, Leyton JV. Targeted molecular therapeutics for bladder cancer-a new option beyond the mixed fortunes of immune checkpoint inhibitors? *Int J Mol Sci*. 2020;21(19):7268. doi:10.3390/ijms21197268
14. Azari F, Zhang K, Kennedy GT, et al. Precision surgery guided by intraoperative molecular imaging. *J Nucl Med*. 2022;63(11):1620–1627. doi:10.2967/jnumed.121.263409
15. Wan H, Du H, Wang F, Dai H. Molecular imaging in the second near-infrared window. *Adv Funct Mater*. 2019;29(25). doi:10.1002/adfm.201900566
16. Kessel D. Critical PDT theory III: events at the molecular and cellular level. *Int J Mol Sci*. 2022;23(11):6195. doi:10.3390/ijms23116195
17. Wang F, Zhong Y, Bruns O, Liang Y, Dai H. In vivo NIR-II fluorescence imaging for biology and medicine. *Nat Photonics*. 2024;18:535–547.
18. Zhu S, Tian R, Antaris AL, Chen X, Dai H. Near-infrared-II molecular dyes for cancer imaging and surgery. *Adv Mater*. 2019;31(24):e1900321. doi:10.1002/adma.201900321
19. Ren F, Wang F, Baghdasaryan A, et al. Shortwave-infrared-light-emitting probes for the in vivo tracking of cancer vaccines and the elicited immune responses. *Nat Biomed Eng*. 2023;8(6):726–739. doi:10.1038/s41551-023-01083-5
20. Wang F, Qu L, Ren F, et al. High-precision tumor resection down to few-cell level guided by NIR-IIb molecular fluorescence imaging. *Proc Natl Acad Sci USA*. 2022;119(15):e2123111119. doi:10.1073/pnas.2123111119
21. Tian Y, Shen H, Li L, et al. Enhancing surgical outcomes: accurate identification and removal of prostate cancer with B7-H3-targeted NIR-II molecular imaging. *Eur J Nucl Med Mol Imaging*. 2024;51(9):2569–2582. doi:10.1007/s00259-024-06714-w
22. Wang B, Tang C, Lin E, et al. NIR-II fluorescence-guided liver cancer surgery by a small molecular HDAC6 targeting probe. *EBioMedicine*. 2023;98:104880. doi:10.1016/j.ebiom.2023.104880
23. Li C, Mi J, Wang Y, et al. New and effective EGFR-targeted fluorescence imaging technology for intraoperative rapid determination of lung cancer in freshly isolated tissue. *Eur J Nucl Med Mol Imaging*. 2023;50(2):494–507. doi:10.1007/s00259-022-05975-7
24. Guo X, Li C, Jia X, et al. NIR-II fluorescence imaging-guided colorectal cancer surgery targeting CEACAM5 by a nanobody. *EBioMedicine*. 2023;89:104476. doi:10.1016/j.ebiom.2023.104476

25. Cheng Z, Jin Y, Li J, et al. Fibronectin-targeting and metalloproteinase-activatable smart imaging probe for fluorescence imaging and image-guided surgery of breast cancer. *J Nanobiotechnol*. 2023;21(1):112. doi:10.1186/s12951-023-01868-5
26. Derks YHW, Schilham MGM, Rijpkema M, et al. Imaging and photodynamic therapy of prostate cancer using a theranostic PSMA-targeting ligand. *Eur J Nucl Med Mol Imaging*. 2023;50(9):2872–2884. doi:10.1007/s00259-023-06224-1
27. Kularatne SA, Thomas M, Myers CH, et al. Evaluation of novel prostate-specific membrane antigen-targeted near-infrared imaging agent for fluorescence-guided surgery of prostate cancer. *Clin Cancer Res*. 2019;25(1):177–187. doi:10.1158/1078-0432.CCR-18-0803
28. Wu LL, Zhao Q, Wang Q, et al. Membrane dual-targeting probes: a promising strategy for fluorescence-guided prostate cancer surgery and lymph node metastases detection. *Acta pharmaceutica Sinica B*. 2023;13(3):1204–1215. doi:10.1016/j.apsb.2022.07.018
29. Yin C, Zhang H, Sun B, et al. Remarkable suppression of vibrational relaxation in organic semiconducting polymers by introducing a weak electron donor for improved NIR-II phototheranostics. *Adv Funct Mater*. 2021;31(47):2106575. doi:10.1002/adfm.202106575
30. Li T, Fu J, Zeng Z, et al. TIMER2.0 for analysis of tumor-infiltrating immune cells. *Nucleic Acids Res*. 2020;48(W1):W509–w514. doi:10.1093/nar/gkaa407
31. Bolis M, Bossi D, Vallerga A, et al. Dynamic prostate cancer transcriptome analysis delineates the trajectory to disease progression. *Nat Commun*. 2021;12(1):7033. doi:10.1038/s41467-021-26840-5
32. Tang Z, Kang B, Li C, Chen T, Zhang Z. GEPIA2: an enhanced web server for large-scale expression profiling and interactive analysis. *Nucleic Acids Res*. 2019;47(W1):W556–w560. doi:10.1093/nar/gkz430
33. Zhou H, Gao Y, Liu Y, et al. Targeted fluorescent imaging of a novel FITC-labeled PSMA ligand in prostate cancer. *Amino Acids*. 2022;54(1):147–155. doi:10.1007/s00726-021-03102-8
34. Huang J, Yao Y, Zhang L, Yan C, Guo Z. "Crossbreeding" NIR-II flavchromene for PSMA-positive prostate cancer detection and image-guided surgery. *Smart Molecules*. 2024;2(3):e20240020. doi:10.1002/smo.20240020
35. Martínez-Jothar L, Doulkeridou S, Schiffelers RM, et al. Insights into maleimide-thiol conjugation chemistry: conditions for efficient surface functionalization of nanoparticles for receptor targeting. *J Control Release*. 2018;282:101–109. doi:10.1016/j.jconrel.2018.03.002
36. Wu TT, Sikes RA, Cui Q, et al. Establishing human prostate cancer cell xenografts in bone: induction of osteoblastic reaction by prostate-specific antigen-producing tumors in athymic and SCID/bg mice using LNCaP and lineage-derived metastatic sublines. *Int J Cancer*. 1998;77(6):887–894. doi:10.1002/(SICI)1097-0215(19980911)77:6<887::AID-IJC15>3.0.CO;2-Z
37. Moon S-H, Yang BY, Kim YJ, et al. Development of a complementary PET/MR dual-modal imaging probe for targeting prostate-specific membrane antigen (PSMA). *Nanomedicine*. 2016;12(4):871–879. doi:10.1016/j.nano.2015.12.368
38. Neviere Z, Blanc-Fournier C, Guizard A-V, et al. Potential of PSMA for breast cancer in nuclear medicine: digital quantitative immunohistochemical analysis and implications for a theranostic approach. *BMC Cancer*. 2024;24(1):1328. doi:10.1186/s12885-024-13065-0
39. Shahid M, Alaofi AL, Alqahtani MS, Syed R. Genetic implications of PSMA expression variability in breast cancer subtypes with a focus on triple-negative breast cancer. *J Appl Genet*. 2024;65(3):505–510. doi:10.1007/s13353-023-00814-3
40. Qin C, Song X, Sun S, et al. [68Ga]Ga-PSMA-617 PET/MRI for imaging patients suspected of hepatocellular carcinoma. *Eur J Nucl Med Mol Imaging*. 2025;52:1278–1290. doi:10.1007/s00259-024-06973-7
41. Dorff TB, Fanti S, Farolfi A, Reiter RE, Sadun TY, Sartor O. The evolving role of prostate-specific membrane antigen-based diagnostics and therapeutics in prostate cancer. *Am Soc Clin Oncol Educ Book*. 2019;39:321–330. doi:10.1200/EDBK_239187
42. Wang H, He Z, Liu X-A, et al. Advances in Prostate-Specific Membrane Antigen (PSMA)-targeted phototheranostics of prostate cancer. *Small Struct*. 2022;3(8):2200036. doi:10.1002/sstr.202200036
43. Ao J, Shao X, Liu Z, et al. stimulated raman scattering microscopy enables Gleason scoring of prostate core needle biopsy by a convolutional neural network. *Cancer Res*. 2023;83(4):641–651. doi:10.1158/0008-5472.CAN-22-2146
44. Bravaccini S, Puccetti M, Bocchini M, et al. PSMA expression: a potential ally for the pathologist in prostate cancer diagnosis. *Sci Rep*. 2018;8(1):4254. doi:10.1038/s41598-018-22594-1
45. Zhang J, Rakhimbekova A, Duan X, et al. A prostate-specific membrane antigen activated molecular rotor for real-time fluorescence imaging. *Nat Commun*. 2021;12(1):5460. doi:10.1038/s41467-021-25746-6
46. Wang J, Zang J, Wang H, et al. Pretherapeutic 68Ga-PSMA-617 PET may indicate the dosimetry of 177Lu-PSMA-617 and 177Lu-EB-PSMA-617 in main organs and tumor lesions. *Clin Nucl Med*. 2019;44(6):431–438. doi:10.1097/RLU.0000000000002575
47. Pernthaler B, Kulnik R, Gstettner C, Salamon S, Aigner RM, Kvaternik H. A prospective head-to-head comparison of 18F-fluciclovine with 68Ga-PSMA-11 in biochemical recurrence of prostate cancer in PET/CT. *Clin Nucl Med*. 2019;44(10):e566–e573. doi:10.1097/RLU.0000000000002703
48. Berrens AC, Knipper S, Marra G, et al. State of the art in prostate-specific membrane antigen-targeted surgery-a systematic review. *Eur Urol Open Sci*. 2023;54:43–55. doi:10.1016/j.euros.2023.05.014
49. Schottelius M, Wurzer A, Wissmiller K, et al. Synthesis and preclinical characterization of the PSMA-targeted hybrid tracer PSMA-I&F for nuclear and fluorescence imaging of prostate cancer. *J Nucl Med*. 2019;60(1):71–78. doi:10.2967/jnumed.118.212720
50. Urso L, Rocca GC, Conti GM, et al. 68Ga-PSMA-11 PET/CT in bilateral clear cell renal cell carcinoma: an intra-patient comparison between high and low grade tumors. *Nuclear Med Mol Imag*. 2023;57(6):298–300. doi:10.1007/s13139-023-00805-6
51. Wang Z, Tian R, Niu G, et al. Single low-dose injection of Evans blue modified PSMA-617 radioligand therapy eliminates prostate-specific membrane antigen positive tumors. *Bioconjugate Chem*. 2018;29(9):3213–3221. doi:10.1021/acs.bioconjchem.8b00556
52. Zang J, Wang G, Zhao T, et al. A Phase 1 trial to determine the maximum tolerated dose and patient-specific dosimetry of [(177)Lu]Lu-LNC1003 in patients with metastatic castration-resistant prostate cancer. *Eur J Nucl Med Mol Imaging*. 2024;51(3):871–882. doi:10.1007/s00259-023-06470-3
53. Kennedy GT, Azari FS, Bernstein E, et al. A prostate-specific membrane antigen-targeted near-infrared conjugate for identifying pulmonary squamous cell carcinoma during resection. *Mol Cancer Ther*. 2022;21(4):546–554. doi:10.1158/1535-7163.MCT-21-0821
54. Stibbe JA, de Barros HA, Linders DGJ, et al. First-in-patient study of OTL78 for intraoperative fluorescence imaging of prostate-specific membrane antigen-positive prostate cancer: a single-arm, phase 2a, feasibility trial. *Lancet Oncol*. 2023;24(5):457–467. doi:10.1016/S1470-2045(23)00102-X
55. Zhang L, Shi X, Li Y, et al. Visualizing Tumors in Real Time: a Highly Sensitive PSMA Probe for NIR-II Imaging and Intraoperative Tumor Resection. *J Med Chem*. 2021;64(11):7735–7745. doi:10.1021/acs.jmedchem.1c00444
56. Voskuil FJ, Vonk J, van der Vegt B, et al. Intraoperative imaging in pathology-assisted surgery. *Nat Biomed Eng*. 2022;6(5):503–514. doi:10.1038/s41551-021-00808-8

57. Zeng F, Li C, Wang H, et al. Intraoperative resection guidance and rapid pathological diagnosis of osteosarcoma using B7H3 targeted probe under NIR-II fluorescence imaging. *Adv Sci*. 2024;11(33):e2310167. doi:10.1002/advs.202310167
58. Zhang Z, Du Y, Shi X, et al. NIR-II light in clinical oncology: opportunities and challenges. *Nat Rev Clin Oncol*. 2024;21(6):449–467. doi:10.1038/s41571-024-00892-0
59. Zhang NN, Lu CY, Chen MJ, et al. Recent advances in near-infrared II imaging technology for biological detection. *J Nanobiotechnol*. 2021;19(1):132. doi:10.1186/s12951-021-00870-z